Journal of
Materials Chemistry C

ROYAL SOCIETY
OF CHEMISTRY

PAPER

View Article Online
View Journal | View Issue

Check for updates

Cite this: *J. Mater. Chem. C*, 2024, **12**, 5568

Structured carbon nanotube–elastomer nanocomposites with a morphing–contact mechanism for an advanced underwater perception warning system†

Feng Deng,[ab] Peng Xiao,[*ab] Wei Zhou,[ab] Qing Yang[cd] and Tao Chen[*ab]

Received 19th January 2024,
Accepted 14th March 2024

DOI: 10.1039/d4tc00284a

rsc.li/materials-c

Underwater sensors with high sensitivity in danger sensing and warning ability have become an urgent requirement for various underwater applications. We prepared flexible, transferable, and tailorable conductive Janus films through the morphology manipulation of an air–water interface. Herein, the interface-guided elastic conductive Janus films were rationally designed to construct floating underwater sensors, in which a bilayer structure was integrated with the Janus films in self-supported and supported forms. The as-prepared underwater sensor achieved both high sensitivity sensing *via* 3D morphing and depth/intensity threshold warning ability through dynamic film contacts. When the depth or flow field strength was stronger than a preset threshold, the morphing film could contact with the supported film, resulting in the reversal of the current signal for danger warning. Furthermore, a wearable sensor was designed to efficiently monitor a swimmer who dives to unsafe depths or struggles with drowning risk.

Introduction

Oceans cover more than 70% percent of the earth and are rich in marine organisms, mineral resources, *etc.* Marine sensory systems have played significant roles in underwater communication, resource exploration and environmental protection.[1–5] The development of flexible underwater sensory materials and related wearable devices[6–9] has aroused extensive attention for use in harsh environments and extreme application scenarios. However, compared with conventional flexible sensors that work in the air environment,[10–12] rigorous requirements in terms of material composition, surface wettability and device structure are needed for underwater sensory systems.[13–15] To date, extensive efforts have been dedicated to developing functional hydrogels,[16] ionogels,[17] superhydrophobic aerogels,[18] waterproof conductive fabrics[19] and piezoresistive[20] and piezoelectric[21] electronic devices for underwater sensing applications.

Optical camouflage ionogels, which are typical examples of such materials, employ ion–dipole and ion–ion interactions and have demonstrated favourable underwater sensing performance when applied in wearable and contactless sensory systems.[22] Furthermore, superhydrophobic conductive WS_2-nanosheets-wrapped aerogel, have the advantages of detecting tiny underwater vibrations based on the piezoresistive mechanism.[23]

Moreover, the introduction of piezoelectricity in underwater wearable sensors enabled effective and wireless communication.[24] Marine organisms have the capabilities of sensitive perception, danger capturing and further self-protection.[25–27] While recent reports have focused on contact-based and contactless underwater sensing functions, the capability of signalling danger is urgently desired. More recently, Lai *et al.* reported a series of novel wearable underwater sensing and rescue devices (*e.g.*, superhydrophobic knitted fabric,[28] flexible MXene-based hydrogels,[29] *etc.*) to realize human–robot interaction for underwater rescue. However, achieving creature-like smart sensory systems with integrated high-sensitivity underwater sensing and danger-warning capabilities remains a challenge.

Human beings have biological structures designed for specific functions. Organelle membranes in cells can deform under external stimuli and further contact each other, forming membrane contact sites (MCSs)[30] for organelle communication. MCSs are crucial for coordinating cellular functions and

---

[a] *Key Laboratory of Advanced Marine Materials, Ningbo Institute of Materials Technology and Engineering, Chinese Academy of Sciences, Ningbo 315201, China. E-mail: xiaopeng@nimte.ac.cn, tao.chen@nimte.ac.cn*
[b] *School of Chemical Sciences, University of Chinese Academy of Sciences, Beijing, 100049, China*
[c] *State Key Laboratory of Modern Optical Instrumentation, College of Optical Science and Engineering, International Research Center for Advanced Photonics, Zhejiang University, Hangzhou, 310027, China*
[d] *Research Center for Intelligent Sensing, Zhejiang Lab, Hangzhou, 311100, China*

† Electronic supplementary information (ESI) available. See DOI: https://doi.org/10.1039/d4tc00284a

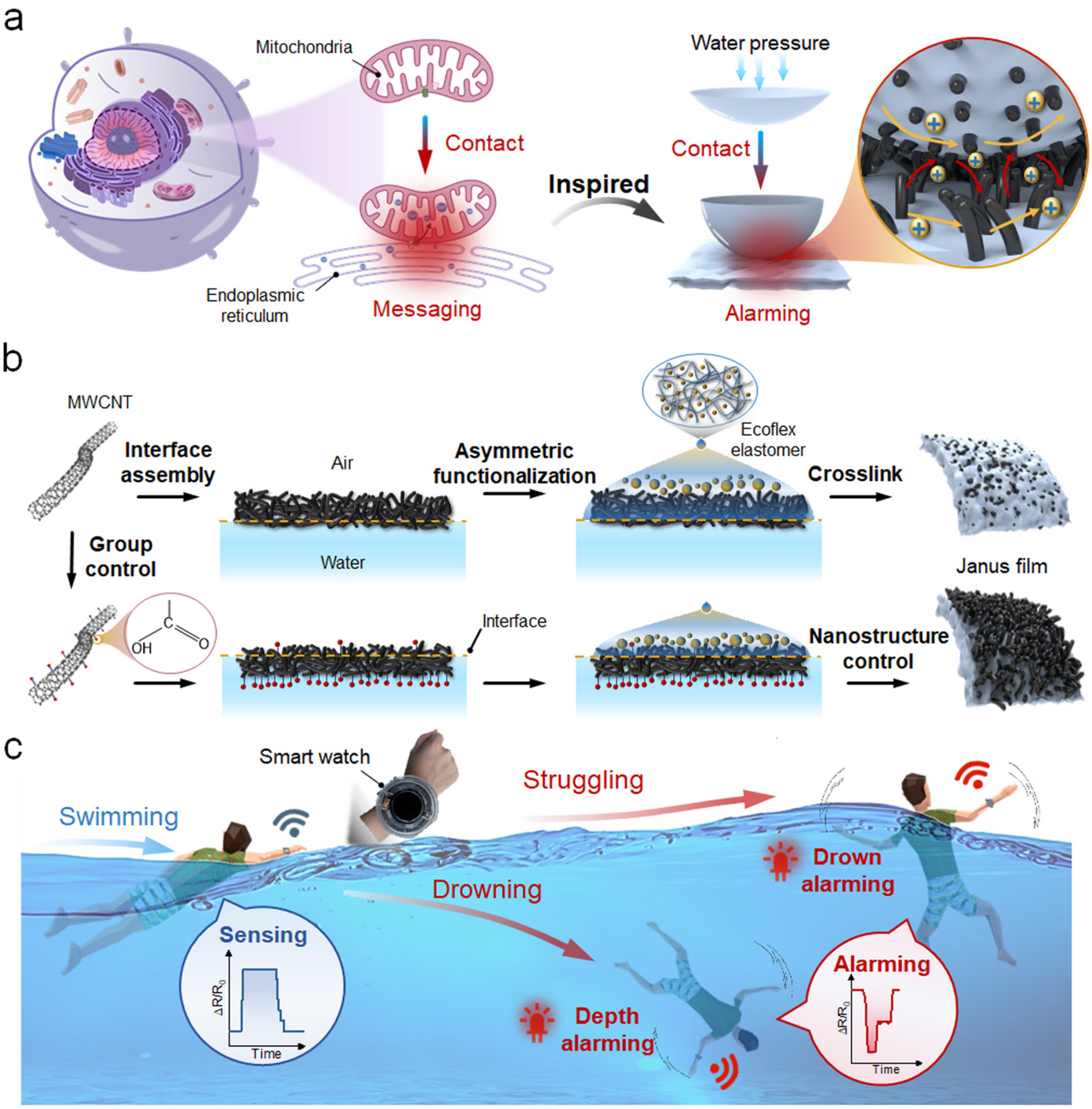

Scheme 1 (a) Schematic illustration of interface morphing and the contact mechanism of the floating-structure sensor inspired by the membrane contact and messaging between mitochondria and ER in a cell. (b) Schematic of the microstructure of the Ecoflex-based Janus films fabricated using MWCNTs with or without the –COOH groups at the water–air interface. (c) The illustration of the smart-watch for underwater sensing and danger alarm signalling in unsafe water depth and early drowning scenarios.

cell response to physiological and pathological stimuli. For instance, membrane contact between the endoplasmic reticulum (ER) and mitochondria plays a crucial role in shaping cellular Ca^{2+} flux by transmitting certain messages within the cell,[31] as shown in Scheme 1a. Inspired by the membrane deformation–contact interaction behavior involved in intracellular communications, a floating structure-enabled underwater sensor was rationally designed in this work by combining self-supported and supported elastic conductive Janus films to form a face-to-face structure. Fabricated by interfacial dispersion and self-assembly, the multi-walled carbon nanotubes (MWCNTs) film functionalized with –COOH groups manifested a discernible contrast in wettability between its air- and water-facing surfaces.[32] As illustrated in Scheme 1b, the CNT side of the Janus film generated using unmodified MWCNTs exhibited lower exposure than its counterpart fabricated using MWCNTs with –COOH groups. The results of the 3D film morphing studies and further exploration of the contact mechanism exemplify that the achieved underwater sensor can sensitively detect water depth and wave stimuli and effectively signal danger. Furthermore, the integration of a microprocessor controller into the sensor allowed the formation of a closed-loop system, enabling active sensing and warning of danger thresholds, such as dangerous depths and strong sea waves. As a proof of concept, a smartwatch was constructed (Scheme 1c) to demonstrate its potential in real-time monitoring of swimming behavior, diving water depth, and abnormal struggling, as well as actively providing warning feedback for water rescue.

Experimental section

Materials

Raw carbon nanotubes (CNTs) (diameter: 20–30 nm; length, 10–30 μm; –COOH content: about 1.23 wt%) with a purity of over 98% were purchased from Chengdu Organic Chemistry Co., Ltd. The CNTs were rinsed thoroughly with anhydrous ethanol before use. Silicon rubber (Ecoflex$^{\text{TM}}$ 00-50) was purchased from Smooth-on, USA (the ratio between components A and B was 1 : 1) and dissolved using *N*-heptane with a weight ratio of 9.18%. General chemicals of reagent grade were used as received from Sinopharm Chemical Reagents. Anhydrous ethanol and deionized water were used as rinsing solvents.

Preparation of the CNTs membrane

First, the CNT powder (500 mg) was dispersed in anhydrous ethanol (250 mL). This was followed by ultrasonication (250 W) for 6 h to form a uniform and stable dispersion. Subsequently, the resultant dispersion (35 mL) was spread onto the water surface by spray-coating in a round glass container (diameter: 25 cm), and a relatively uniform preassembled membrane was formed at the air/water interface. After stabilization for about 10 min, a porous sponge was placed on one side of the interface to quickly siphon water from the system, causing the area of the preassembled membrane to decrease significantly. In this process, the homogeneous pre-assembled CNT film was closely packed toward the direction opposite the siphon direction. When the porous sponge could not drive the membrane to move any further, the desired membrane was ultimately formed.

Preparation of the CNTs/Ecoflex film

The Ecoflex precursor (A and B was 1 g : 1 g) was diluted with heptane (30 mL) and dispersed uniformly by ultrasonication for 5 min. Then, the Ecoflex dispersion was spread onto the CNT film by drop coating with a burette, followed by a typical Ecoflex curing (crosslinking) process at 25 °C. When the cross-linking time reached 6 h, the CNTs/Ecoflex Janus film was formed. These films were used to conduct further experiments.

Preparation of the underwater sensor

At first, a hole of appropriate diameter was cut out in the middle of a Petri dish, and then an ultrathin layer of PDMS prepolymer was scraped on its surface. The prepared CNTs/Ecoflex Janus film was transferred onto the surface of the Petri dish with part of the film attached to the substrate and the other part self-supported. Another film was transferred directly onto the surface of a circular plastic substrate and adhered closely to it. After curing the PDMS prepolymer layer at 60 °C for 1 h, the film was closely attached to the substrate. Then, the CNT sides of the two films were joined using copper tape in a 60 °C oven with the aid of silver paste and curing in order to form a conductive circuit that can be connected to wires. Another Petri dish acted as a waterproof cover for the entire conductive circuit, and the setup was sealed using a waterproof adhesive, ultimately resulting in an underwater sensor with a floating structure.

Characterization and measurements

The surface and cross-section morphologies of the film were observed using a Hitachi-S4800 field-emission scanning electron microscope (FE-SEM) operated at an accelerating voltage of 4 kV. Raman scattering measurements were carried out on an R-3000HR spectrometer (Raman Systems, Inc., R-3000 series) with a solid-state diode laser (532 nm) for excitation in the wavenumber range of 3500–200 cm^{-1}. A Z1 Zwick/Roell Universal Testing System was used to test the stress–strain characteristics of the films. When the sensor was used to detect underwater depth or external stimuli, the electrodes at both ends of the sensor were connected to an electrochemical workstation through wires, and the electrochemical workstation was connected to the computer. An electrochemical Workstation (CH Instruments, CHI660E, Chenhua Co., Shanghai, China) was used to record the real-time current (I) at a constant voltage (V_0) of 1 V, while the real-time resistance (R) was calculated using the equation $R = V_0/I$.

Results and discussion

Microstructure control in the Janus films and the structural design of the underwater sensor

Owing to the favourable conductive and elastic/morphable characteristics of carbon nanomaterial/elastomer-based Janus films,[33,34] a typical Janus film (MWCNTs/Ecoflex) was employed in our system. The MWCNTs/Ecoflex-based Janus film was constructed at the air/water interface using the CNT self-assembly strategy and *in situ* interfacial asymmetric functionalization of the Ecoflex elastomer (Scheme 1b).[35] An extensive comparison of the morphology of Janus films derived from two variants of MWCNTs, namely unmodified MWCNTs and MWCNTs with –COOH groups, was conducted. This comprehensive analysis encompassed a detailed examination of the microstructure of individual MWCNTs; a schematic representation delineating the architecture of the Janus films and the high-resolution scanning electron microscopy (SEM) images are depicted in Fig. 1a. As shown in Fig. 1b, the as-prepared Janus film presented a typical wrinkled macroscopic morphology under mechanical stretch. The SEM image showed the asymmetric structure of the Janus film (Fig. 1c). In addition, the air side of the Janus film with pure Ecoflex had a smooth morphology (Fig. S1, ESI†). As seen in Fig. S2 (ESI†), by manipulating the amount of Ecoflex precursor added, the height of exposed COOH-MWCNTs could be modified. Fig. S3 (ESI†) illustrates the modulation of COOH-MWCNT spatial density with variations in dispersion concentration during membrane fabrication, thereby exemplifying its influence on the morphological features of COOH-MWCNTs. In electrical testing (Fig. S4, ESI†), resistance in the Janus film reduced as the dispersion concentration of COOH-MWCNTs increased. Moreover, the Raman spectra were obtained to characterize the chemical composition of the Janus film. As displayed in Fig. 1d, the CNTs side showed typical characteristic peaks of CNTs (D, G and 2D peaks of CNTs at 1349, 1580 and 2692 cm^{-1}, respectively) and Ecoflex (low frequency: 488 and 707 cm^{-1};

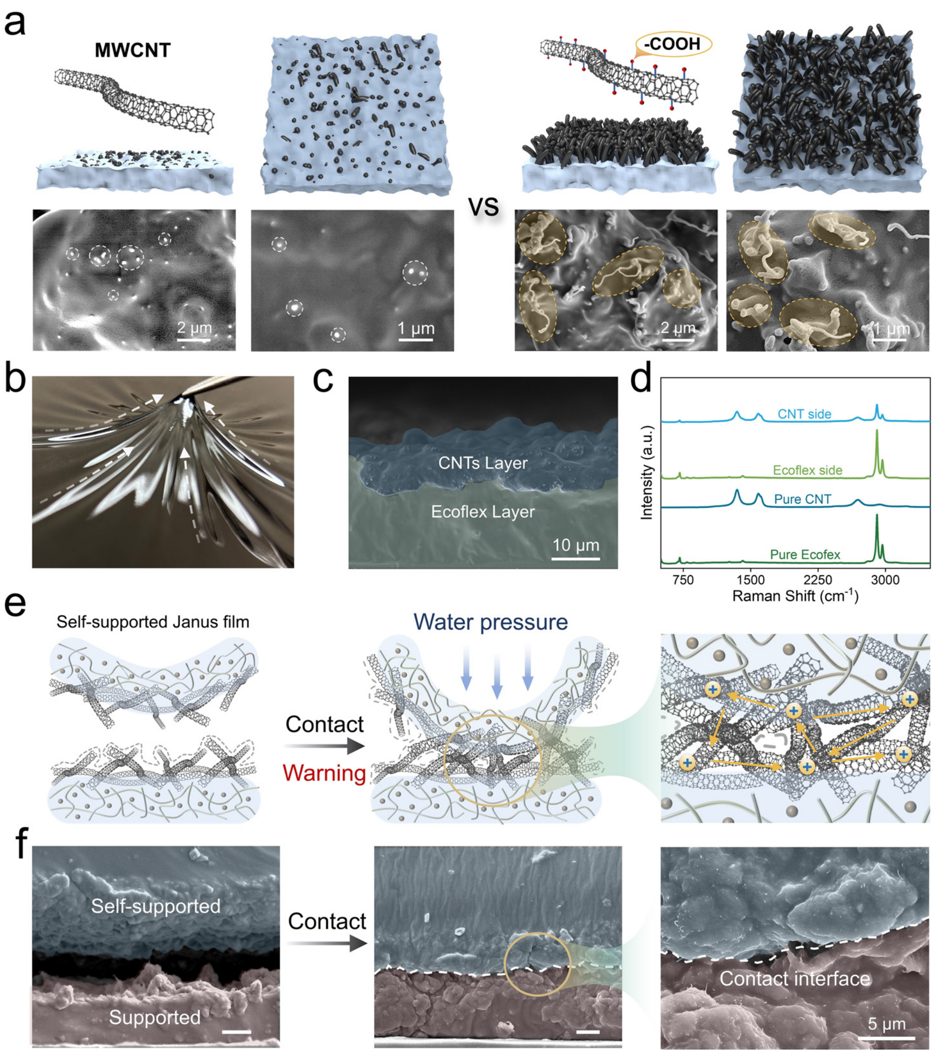

Fig. 1 (a) Comparison of the morphology of the Janus films prepared using unmodified MWCNTs and MWCNTs with –COOH groups, including the microstructure of a single MWCNT, the schematic diagram of the Janus films and SEM photographs. (b) Photograph of the stretched Janus film. (c) Cross-sectional SEM image of the Janus film. (d) Raman spectra of both sides of the MWCNTs/Ecoflex Janus film, pure MWCNTs and the pure Ecoflex membrane. (e) Schematics of contact behavior and hole flow in the two as-prepared Janus films inspired by the morphological changes and messaging at MCSs. (f) SEM images of the two Janus films before and after contact. Bar: 5 µm.

high frequency: 2904 and 2962 cm^{-1}). Meanwhile, the Ecoflex side of the Janus film presented the characteristic peaks of pure Ecoflex. Owing to the asymmetric introduction of CNTs in the assembled film, the mechanical strength of the achieved Janus film was relatively higher than that of the pure Ecoflex elastomer (Fig. S5 and S6, ESI†).

In biological systems, membrane contacts are considered important channels that facilitate information communication. Based on this mechanism, a biomimetic 3D morphing sensory system was rationally designed using the self-supported/morphable and supported Janus films for the achievement of underwater sensory and alarm functions based on dynamic 3D deformation actuated by water pressure (Fig. 1e). Especially, with the increase in the deformation of the self-supported film, the corresponding MWCNTs formed the new conductive paths by the flow of holes after the contact of the two Janus films. When the self-supported Janus film came in contact with the supported Janus film, the squeeze between the films caused the holes to flow continuously (Fig. 1f).

Performance of the Janus film in sensing and the deformation of the underwater sensor

The sensing performance of the Janus film was further characterized. Typical plots of the CNTs/Ecoflex Janus film were tested at different loading conditions based on the change in normalized resistance ($\Delta R/R_0$):

$$\frac{\Delta R}{R_0} = \frac{R - R_0}{R_0} \tag{1}$$

where R represents real-time resistance, and R_0 is the initial resistance at the relaxed state (the Janus film strip was 20 × 5 mm in size (length × width)). Notably, the output electrical signals remained stable at typical frequencies from 0.1 to 5 Hz (Fig. S7, ESI†, strain: 10%). The real-time variation of normalized resistance was measured under different stretching strain cycles (from ε = 1, 2, 4, 6, 8, to 10%), as shown in Fig. S8 (ESI†), which represents the sensitive and reversible response of the sensing signal. As displayed in Fig. S9 (ESI†), normalized resistance showed a stable and sensitive response to applied strain even up to 2000 stretching and release cycles. Based on the aforementioned analysis, the Janus film shows stable and sensitive underwater sensing performance.

To achieve the 3D morphing system, the Janus film was conformally attached to the hollow surface of a self-supported film, which could be actuated to morph in 3D from the flat state to the expanded state using pressured air (Fig. 2a). A typical self-supported Janus film with a diameter of 25 mm was employed to observe the real-time variation in normalized resistance under a series of frequencies (from 0.1 to 1 Hz) (Fig. 2b). As displayed in Fig. 2c, the normalized resistance showed a stable and sensitive response to applied strain over 500 expansion and release cycles (pressure: 16 kPa, frequency: 1 Hz). Fig. S10 in ESI† shows the extent of deformation of the self-supported Janus film under different pressures. In addition, the normalized resistance of the self-supported Janus film was tested at applied pressures of 0, 4, 8, 12, and 16 kPa, respectively (Fig. 2d). The area strain and expansion of self-supported Janus films with different diameters were proportional to the applied pressure *i.e.* 4, 8, 12, and 16 kPa (Fig. 2e and f). With the increase in hollow diameter, the area strain and expansion amplitude of the self-supported Janus film exhibited a gradual decreasing tendency under fixed pressure.

To construct the underwater sensor, a bilayer structure was rationally designed, as shown in Fig. 2g. In this system, the Janus films remained self-supported on a hollow substrate and supported on a solid substrate. In the integrated sensory system, the conductive layers of these two Janus films were placed in a face-to-face configuration, enabling the formation of a conductive contact under water pressure. Based on the aforementioned mechanism, the self-supported film in the prepared underwater sensor can experience gradual 3D deformation while transitioning from the uncontacted to contacted states driven by water pressure (Fig. 2h). Prior to reaching the contacted mode, the 3D deformation of the floating film can induce corresponding resistance changes in the series circuit. When the two films form a typical contact, the circuit system would experience a transition from a series circuit to a parallel mode (Fig. S11, ESI†), resulting in a sharp change in the sensory signals.

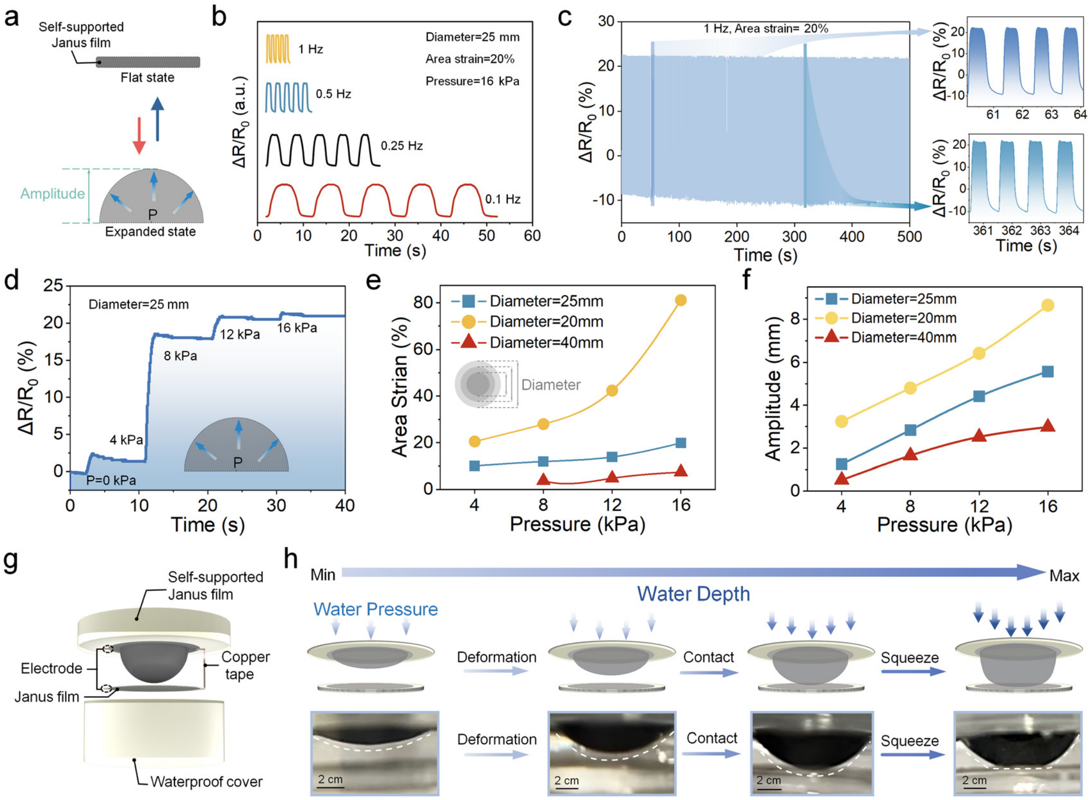

Fig. 2 (a) Diagram of the initial flat state and the expanded state of the self-supported Janus film under pressured air. (b) Normalized resistance *versus* time curves of a 25-mm circular self-supported Janus film under an applied pressure of 16 kPa at different frequencies. (c) The normalized resistance *versus* time curve of 500 cycles under an applied pressure of 16 kPa (frequency: 1 Hz, area strain: 20%). (d) The normalized resistance *versus* applied pressure curve of a 25-mm circular self-supported Janus film under 0, 4, 8, 12, and 16 kPa. (e) Area strain and (f) amplitude changes of 20-, 25- and 40-mm circular self-supported Janus films under applied pressure of 4, 8, 12, and 16 kPa. (g) Structural disassembly diagram of the underwater sensor, including the self-supported Janus film, electrodes, copper tape, Janus film and waterproof cover. (h) Schematic illustrations and photographs of the changing morphology of the self-supported film and the supported film in the sensor under water pressure changes with increasing depth.

Underwater depth sensing and triggering alarm

When the self-supported film was exposed to the underwater environment, it experienced gradual 3D morphing with the increase in water depth. As displayed in Fig. 3a, the self-supported film could sensitively deform based on water pressure. With the increase in water depth from 0 to 1.3 m, the real-time current from the self-supported Janus thin film presented a step-by-step decrease, showing a sensitive and stable response to water depth. Once the sensor reached the threshold depth of 1.4 m, the current increased rapidly and also demonstrated a typical stepped increase from 1.4 to 1.7 m. Moreover, the corresponding normalized resistance *versus* depth curve clearly demonstrated that it experienced a reverse transition of normalized resistance from positive to negative values (Fig. 3b).

When the sealed sensor was applied in water, the self-supported Janus film was subjected to force, as depicted in Fig. 3c. The combined force (F) of film gravity (G), the upward pressure of the air cavity on the Janus film (F_{Air}) and the downward pressure of water on the Janus film (F_{Water}) was calculated according to the equation:

$$F = G + F_{\mathrm{Water}} - F_{\mathrm{Air}} \tag{2}$$

where F_{Water} is dependent on the depth and influences the morphing of the elastic Janus film according to the equation:

$$F_{\mathrm{Water}} = \frac{\rho g H}{S} \tag{3}$$

where ρ is the density of water, g is gravitational acceleration, H is the depth of the sensor, and S is the area of the self-supported film in contact with water.

Based on reversible 3D morphing and the subsequent film contact behaviors, the underwater sensor could achieve

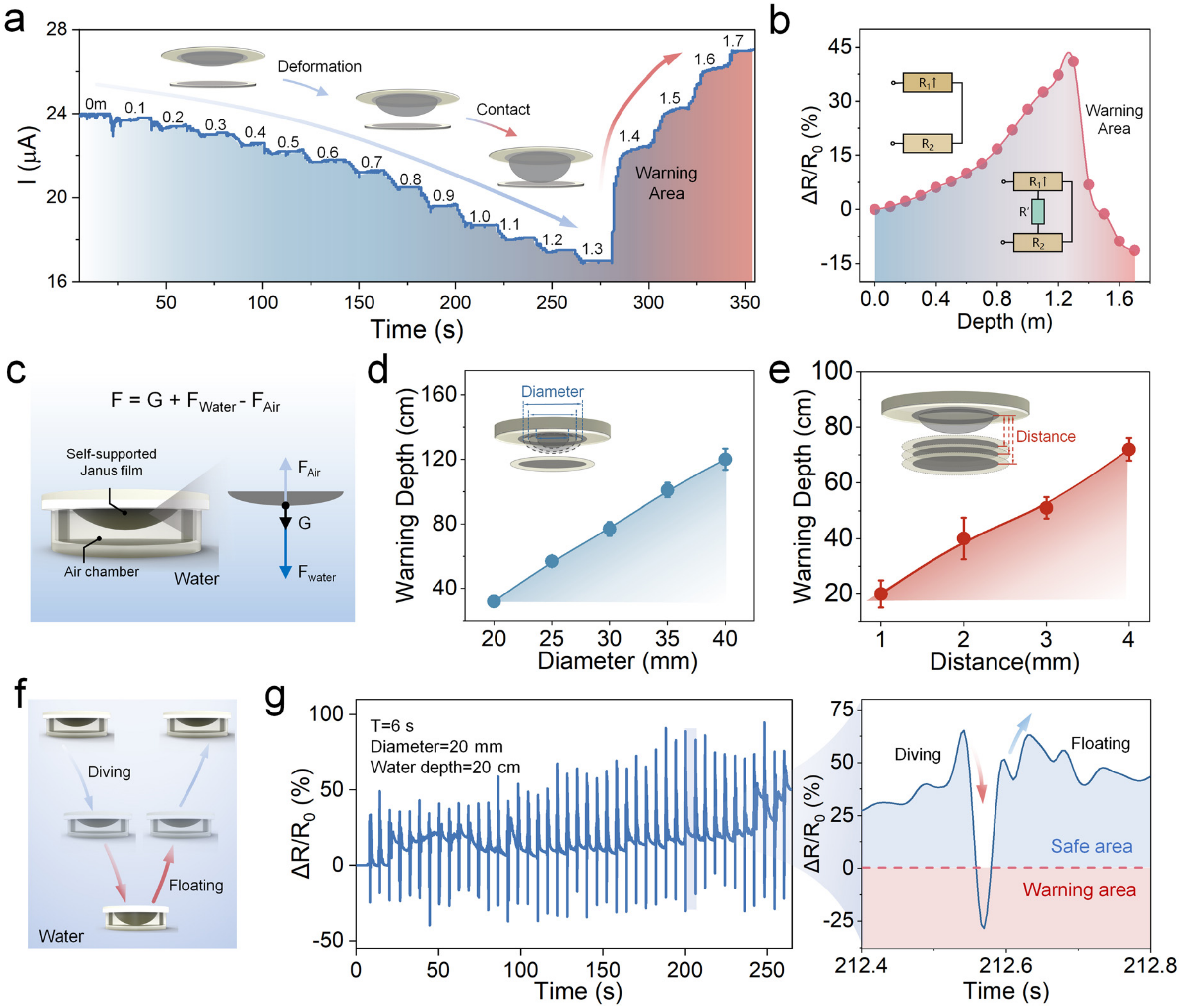

Fig. 3 (a) Current *versus* time curve of a 40-mm diameter sensor with increasing depth of descent; a steep increase in current occurs at a depth of 1.3–1.4 m. (b) The normalized resistance *versus* time curve of a 40-mm diameter sensor at varying depths of descent (from 0 to 1.7 m). (c) Analysis of the forces acting on the self-supported film of the underwater sensor. (d) The warning depths correspond to the diameters of the self-supported layer in the underwater sensors (distance: 4 mm). (e) The warning depths correspond to the distance between the self-supported film and the supported film in the sensors (diameter: 30 mm). (f) Schematic diagram of a cycle of the sensor, including the diving and floating states. (g) The normalized resistance *versus* time curve shows the two states of the underwater sensor over 40 cycles. The enlarged diagram on the right shows the sensor profile while diving into the depths and returning to the surface.

dynamic and reversible sensing and danger warning functions. In this case, the descent depth of the sensor when the normalized resistance turns negative is taken as the warning depth. It is clear from the previous section that the expansion of the self-supported Janus film is negatively related to its diameter when subjected to a force. Therefore, we can fabricate sensors for different warning depths by adjusting these parameters of the sensor. Here, only two parameters, namely the diameter of the self-supported Janus film and the distance between the two conductive MWCNT layers, were considered. For the underwater warning depth test, we compared sensors consisting of self-supported layers with diameters of 20, 25, 30, 35, and 40 mm (distance = 4 mm). A large set of experimental data (Fig. S12, ESI†) was summarized to acquire the results presented in Fig. 3d. Similarly, tests were carried out using sensors with interlayer distances of 1, 2, 3, and 4 mm (diameter = 30 mm), and the data (Fig. S13, ESI†) were summarized to obtain the curve in Fig. 3e. In summary, it is possible to customise the underwater sensor to warning depths ranging from 20 to 120 cm. This demonstrates the great potential of this product for practical application in underwater sensing and warning.

The reversal of the current signal due to contact formation between the self-supported film and the supported film can remarkably change the circuit configuration from a series to a parallel state. As shown in Fig. 3f, the membrane in the underwater sensor experienced a series of motion behaviors while diving into the water, reaching the threshold depth and floating. These motion behaviors were sensitively captured by the sensor as changes in the characteristic current signal, showing good cyclic stability ($T = 6$ s, depth = 20 cm, diameter = 20 mm), as shown in Fig. 3g. The excellent sensing performance of the underwater sensor shows its potential in underwater detection. The characteristic motion could be clearly recognized by the typical normalized resistance curve. In this case, for water depth warning, we defined $\Delta R/R_0 > 0$ as the safety signal and $\Delta R/R_0 < 0$ as danger. Furthermore, we compared the sensing performance of the underwater sensors in water and seawater, as illustrated in Fig. S14 (ESI†). The self-supported film experienced more pressure at equivalent depths in the denser seawater. As a result, the film exhibited a larger deformation, resulting in a slight reduction in the warning depth of the sensor in seawater compared with water. However, in most underwater environments, the normal use of the sensor would not be affected significantly.

Integrated sensory systems for strong wave warning and drowning alarm

This underwater sensory system can be employed to detect mechanical stimuli from the water surface and underwater conditions (Fig. S15 and S16, ESI†). Using our sensory system, an underwater sensor connected to an Arduino module (microprocessor) and a warning LED light was rationally designed to achieve underwater motion monitoring and danger warning (Fig. 4a). Besides, sea waves with different flow velocities ranging from 0.05 m s^{-1} to 0.4 m s^{-1} were simulated, as demonstrated in Fig. 4b and Fig. S17 (ESI†). When the wave velocity reached 0.4 m s^{-1}, the normalized resistance experienced a transition from a positive value to a negative value, demonstrating a typical alarm signal for strong waves.

As a proof of concept, we designed a closed-loop sea wave monitoring system by integrating the microprocessor controller with a warning LED light. When the intensity of the sea wave was higher than the pre-designed danger threshold, the current output showed a rapid increase, triggering the warning LED light (Fig. S18, ESI†). In our system, a beach scene was simulated, in which the sensor was used to monitor the real-time intensity of sea waves. When the intensity of sea waves was lower than the danger threshold, the warning LED light was in a dark state and people could swim inside the sea. Once the sea wave intensity became stronger than the threshold, the contact between the films could light the LED to warn people (Fig. 4c and Video S1, ESI†).

Furthermore, we also demonstrated an advanced application of the underwater wearable device (Fig. 4d). As shown in Fig. 4e and Fig. S19 (ESI†), the sensor was carefully integrated into a smartwatch worn on the arm by the volunteer to test for underwater motion detection. For application in swimming, swimming parameters, such as stroke frequencies (0.25, 0.5 and 1 Hz) and amplitudes (5, 10 and 15 cm), could be sensitively monitored by our sensor. The corresponding changes in normalized resistance with different responsive frequencies and peak values effectively recorded the swimming behaviors of an individual. As illustrated in Fig. 4f, normal swimming, fluttering, drowning in a dangerous area and rescue were completely recorded. More importantly, based on the depth warning mechanism of the sensor, a warning line was pre-engineered to indicate dangerous swimming areas where the swimmer was not safe. The smartwatch could achieve real-time detection of the whole swimming process. In order to further verify the reliability and accuracy of this sensory system in real scenarios, we conducted a motion monitoring test by slapping on outdoor water surfaces. As shown in Fig. S20 (ESI†), the underwater sensors could accurately detect the action of the volunteer slapping the water surface based on the wind-disturbed background signal. This also demonstrates the immense potential and universality of these sensors in various practical scenarios.

In addition, before drowning in a danger zone, detecting the struggling phase of a swimmer is also very important for early rescue. Therefore, a closed-loop system for early drowning warning was designed, in which the swimmer model system in the smartwatch was connected to a warning screen (Fig. 4g). The warning screen in Fig. 4h shows LED lights for different swimmers to monitor their status of swimming in real-time. For instance, the swimmer model is marked as swimmer 4 in the warning screen (Fig. 4i). As shown in Fig. 4j, when the swimmer model performed breaststroke and subsequently demonstrated abnormal struggling, in the closed-loop system, the control voltage first experienced an increase in the normal swimming state (LED off) and subsequently, a sharp decrease, which turned on the LED light (Fig. 4k). According to the LED on the warning screen, the lifeguard can monitor

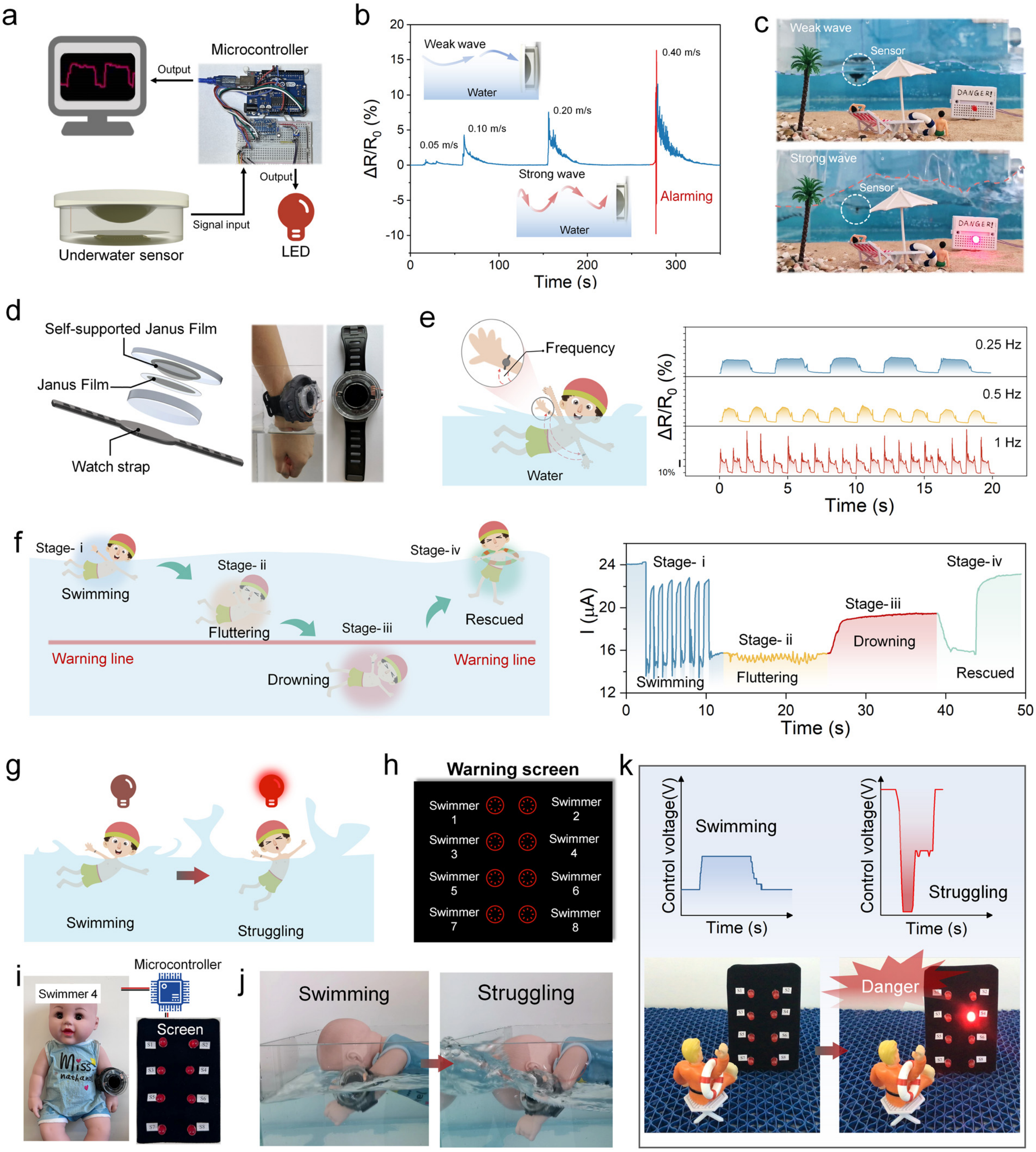

Fig. 4 (a) Schematic of the signal transmission in the underwater sensor. (b) The normalized resistance *versus* time curves of the sensors under fluid fields with various flow rates. The enlarged image on the right is the output signal under a fluid field movement of 0.4 m s^{-1}. Inset: Amplitude changes of the sensor under water flow. (c) Photographs of the weak and strong wave scenarios. (d) Schematic and photos of the wearable sensor. (e) Diagram of the wearable sensor monitoring the frequency (0.25, 0.5 and 1 Hz) of the up and down water-slapping arm movement during swimming and the corresponding normalized resistance *versus* time curves of the sensors. (f) Schematic diagram (left) and real-time signals (right) of the wearable sensor used for monitoring various underwater states. (g) Schematic of scenarios in which the wearable sensor monitors underwater conditions and triggers an alarm, namely swimming and struggling. (h) Diagram of the warning screen to monitor the status of different swimmers in real-time. (i) The components of the closed-loop system that enable real-time motion monitoring of swimmer 4. (j) Photos of the swimmer model showing normal swimming and abnormal struggling. (k) Real-time control voltages (top) and warning screens (bottom) that send immediate danger signals corresponding to the different states (swimming and struggling) of swimmer 4.

the status of swimmers and be ready for rescuing operations (Video S2, ESI†). In practical scenarios, false alarms may occur sporadically. As illustrated in Fig. S21 (ESI†), false alarms can be triggered by slamming into the water surface violently or diving to the warning depth. However, false alarms due to movements beyond the range of normal behaviour and different from the preset actions do not affect the actual use of the sensors.

Conclusion

In this work, we have developed a floating underwater sensor that can integrate both sensitive underwater depth sensing and danger warning enabled by the combination of self-supported and supported elastic conductive thin films. In the context of selecting conductive materials, we crafted conductive films by meticulously controlling the microstructural morphology of MWCNTs at the water–air interface. Based on the 3D morphing mechanism of the film driven by water pressure, this underwater sensor can sensitively capture mechanical stimuli underwater or above the water surface. Furthermore, when the water depth or flow intensity is higher than the threshold, the self-supported film can establish a typical contact with the supported film, triggering a rapid increase in the current signal and thereby resulting in an underwater warning alarm. The proposed 3D morphing–contact mechanism allows the integration of sensitive underwater sensory functions and danger alarm triggers, demonstrating a new strategy for developing underwater sensing and alarm systems.

Author contributions

Feng Deng: data curation, formal analysis, software, visualization and writing – original draft. Peng Xiao: conceptualization, funding acquisition, supervision and writing – review & editing. Wei Zhou: methodology, software and visualization. Qing Yang: resources and supervision. Tao Chen: funding acquisition, supervision and writing – review & editing.

Conflicts of interest

There are no conflicts to declare.

Acknowledgements

This work is supported by National Key Research and Development Program of China (2022YFC2805200), Youth Innovation Promotion Association of Chinese Academy of Sciences (No. 2023313), Natural Science Foundation of China (52373094, 52073295), the Sino-German Mobility Program (M-0424), Key Research Program of Frontier Sciences, Chinese Academy of Sciences (QYZDB-SSWSLH036), Bureau of International Cooperation, Chinese Academy of Sciences (174433KYSB20170061), and K. C. Wong Education Foundation (GJTD-2019-13).

Notes and references

1 J. E. Elliott and K. H. Elliott, *Science*, 2013, **340**, 556–558.
2 K. Sun, W. Cui and C. Chen, *Sensors*, 2021, **21**, 7849.
3 G. Schirripa Spagnolo, L. Cozzella and F. Leccese, *Sensors*, 2020, **20**, 2261.
4 J. Lloret, *Sensors*, 2013, **13**, 11782–11796.
5 J. Wei, P. Xiao and T. Chen, *Adv. Mater.*, 2023, 2211758.
6 J. Wei, Y. Zheng and T. Chen, *Mater. Horiz.*, 2021, **8**, 2761–2770.
7 M. Li, Z. Liu, Y. Hu, R. Li and Y. Cao, *Chem. Eng. J.*, 2023, **472**, 145177.
8 H. Zheng, M. Chen, Y. Sun and B. Zuo, *Chem. Eng. J.*, 2022, **446**, 136931.
9 L. Xu, W. Wang, L. Zhang, D. Wang and A. Zhang, *ACS Appl. Mater. Interfaces*, 2022, **14**, 21623–21635.
10 L. Su, Q. Xiong, Y. Zhu and Y. Zi, *Adv. Funct. Mater.*, 2022, **32**, 2207096.
11 W. Zhou, P. Xiao, Y. Liang, Q. Wang, D. Liu, Q. Yang, J. Chen, Y. Nie, S.-W. Kuo and T. Chen, *Adv. Funct. Mater.*, 2021, **31**, 2105323.
12 S. Li, Y. Zhang, X. Liang, H. Wang, H. Lu, M. Zhu, H. Wang, M. Zhang, X. Qiu, Y. Song and Y. Zhang, *Nat. Commun.*, 2022, **13**, 5416.
13 Z. Wang, H. Zhou, D. Liu, X. Chen, D. Wang, S. Dai, F. Chen and B. B. Xu, *Adv. Funct. Mater.*, 2022, **32**, 2201396.
14 X. Zheng, A. M. Kamat, A. O. Krushynska, M. Cao and A. G. Prakash Kottapalli, *Adv. Funct. Mater.*, 2022, **32**, 2207274.
15 Z. Lan, Y. Wang, K. Hu, S. Shi, Q. Meng, Q. Sun and X. Shen, *Carbohydr. Polym.*, 2023, **306**, 120541.
16 S. Wang, L. Wang, X. Qu, B. Lei, Y. Zhao, Q. Wang, W. Wang, J. Shao and X. Dong, *ACS Appl. Mater. Interfaces*, 2022, **14**, 50256–50265.
17 J. Xu, H. Wang, X. Wen, S. Wang and H. Wang, *ACS Appl. Mater. Interfaces*, 2022, **14**, 54203–54214.
18 Y. Liu, Z. Sheng, J. Huang, W. Liu, H. Ding, J. Peng, B. Zhong, Y. Sun, X. Ouyang, H. Cheng and X. Wang, *Chem. Eng. J.*, 2022, **432**, 134370.
19 X. Qi, H. Zhao, L. Wang, F. Sun, X. Ye, X. Zhang, M. Tian and L. Qu, *Chem. Eng. J.*, 2022, **437**, 135382.
20 Y. M. Yousry, V.-K. Wong, R. Ji, Y. Chen, S. Chen, X. Zhang, D. B. K. Lim, L. Shen and K. Yao, *Adv. Funct. Mater.*, 2023, 2213582.
21 S. Abolpour Moshizi, H. Moradi, S. Wu, Z. J. Han, A. Razmjou and M. Asadnia, *Adv. Mater. Technol.*, 2022, **7**, 2100783.
22 Z. Yu and P. Wu, *Adv. Mater.*, 2021, **33**, 2008479.
23 R. Xu, K. Zhang, X. Xu, M. He, F. Lu and B. Su, *Adv. Sci.*, 2018, **5**, 1700655.
24 Q. Zhang, Y. Wang, D. Li, J. Xie, K. Tao, P. Hu, J. Zhou, H. Chang and Y. Fu, *Adv. Funct. Mater.*, 2023, **33**, 2209667.
25 Å. Flock and J. Wersäll, *J. Cell Biol.*, 1962, **15**, 19–27.
26 X. Zheng, A. M. Kamat, M. Cao and A. G. P. Kottapalli, *Adv. Sci.*, 2022, **10**, 2203062.
27 J. C. Montgomery, C. F. Baker and A. G. Carton, *Nature*, 1997, **389**, 960–963.
28 T. Zhu, Y. Ni, K. Zhao, J. Huang, Y. Cheng, M. Ge, C. Park and Y. Lai, *ACS Nano*, 2022, **16**, 18018–18026.
29 Y. Ni, X. Zang, J. Chen, T. Zhu, Y. Yang, J. Huang, W. Cai and Y. Lai, *Adv. Funct. Mater.*, 2023, 2301127.
30 L. Scorrano, M. A. De Matteis, S. Emr, F. Giordano, G. Hajnóczky, B. Kornmann, L. L. Lackner, T. P. Levine,

L. Pellegrini, K. Reinisch, R. Rizzuto, T. Simmen, H. Stenmark, C. Ungermann and M. Schuldiner, *Nat. Commun.*, 2019, **10**, 1287.

31 A. Raffaello, C. Mammucari, G. Gherardi and R. Rizzuto, *Trends Biochem. Sci.*, 2016, **41**, 1035–1049.

32 Y. Liang, J. Shi, P. Xiao, J. He, F. Ni, J. Zhang, Y. Huang, C.-F. Huang and T. Chen, *Chem. Commun.*, 2018, **54**, 12804–12807.

33 Q. Wang, P. Xiao, W. Zhou, Y. Liang, G. Yin, Q. Yang, S.-W. Kuo and T. Chen, *Nano-Micro Lett.*, 2022, **14**, 62.

34 Y. Liang, P. Xiao, F. Ni, L. Zhang, T. Zhang, S. Wang, W. Zhou, W. Lu, S.-W. Kuo and T. Chen, *Nano Energy*, 2021, **81**, 105617.

35 P. Xiao, J. Gu, C. Wan, S. Wang, J. He, J. Zhang, Y. Huang, S.-W. Kuo and T. Chen, *Chem. Mater.*, 2016, **28**, 7125–7133.